Birth and Growth Kinetics of Brome Mosaïc Virus Microcrystals

Marina Casselyn,* Annette Tardieu,† Hervé Delacroix,* and Stéphanie Finet‡
*BioInformatique Structurale, Centre de Génétique Moléculaire, Centre National de la Recherche Scientifique, Gif-sur-Yvette Cedex, France; and †Laboratoire de Minéralogie et Cristallographie de Paris, Centre National de la Recherche Scientifique, Université Paris VI Pierre et Marie Curie, Paris, France; and ‡European Synchrotron Radiation Facility, BP 220, Grenoble, France

ABSTRACT The early steps of crystal nucleation and growth in Brome Mosaïc virus and polyethylene glycol mixtures were analyzed using time-resolved x-ray scattering (at the European Synchrotron Radiation Facility, Grenoble, France). The system was chosen as a crystallization model since the phase diagram of the macromolecule/polymer mixture was known to present, at high polymer concentration, a solid, precipitated phase made of the synchronized formation of a large number of microcrystals. The precipitation and crystallization of the samples was induced by the controlled mixing of virus and polymer using a stopped-flow device. Appearance and growth of Bragg diffraction peaks were used to follow the crystal nucleation and growth as a function of time, virus and polymer concentration, and polymer size. In all samples, the crystallization starts after a few seconds and proceeds for ~1–20 min until there is almost no virus left in the solution. The crystalline system was found to be face-centered cubic, with a unit cell size of 391 Å. The data analysis allowed us to show the presence of viruses in only two states, in solution or in crystals, revealing that the formation of periodic order proceeds without any detectable intermediate amorphous state.

INTRODUCTION

The limiting step in x-ray protein crystallography remains nucleation and crystal growth, the mechanisms of which are not yet completely understood and thus rather poorly controlled. In particular, the earliest steps necessary to make a nucleus, which will grow into a well-developed crystal, are just becoming accessible. In a previous work (Casselyn et al., 2001) the Brome Mosaïc virus (BMV) was used to study with small-angle x-ray scattering (SAXS) the influence of salt and polyethylene glycol (PEG) on the crystallization of large macromolecules. The BMV is an icosahedral plant virus of 264 Å in diameter and a molecular weight of 4.6×10^6 Da, made of a $T = 3$ protein capsid surrounding a RNA genome. In the course of the SAXS study on this virus, Bragg diffraction peaks were observed from the solid phase that precipitates out of the solution when a high concentration of PEG is added, demonstrating that the precipitates were microcrystals. The phenomenon had occurred during the few minutes necessary to prepare our samples, inject them into the sample holder, and record an x-ray spectrum. The microcrystalline precipitates were obtained when using PEG, either alone or combined with salts. The position of the diffraction peaks was conserved, whatever the PEG size, or the presence of salt, revealing that the crystalline system was the same. The system was therefore particularly suited to analyze the first steps of macromolecular nucleation and growth.

PEG is a nondenaturing agent that was used in the past to precipitate viruses as a purification process, and is now in the process to become the most utilized crystallizing agent. After the initial proposal by George and Wilson (1994) that crystallization occurs in a narrow range of second virial coefficients, it is now well established that crystallization occurs in or close to attractive regimes (see Finet et al., 2003). The attraction allows macromolecules to come close to each other and experience contacts. The addition of neutral polymers to colloid solutions results in a nonspecific attractive potential between colloids, called the depletion attraction, dependent upon polymer size and concentration (Asakura and Oosawa, 1958; Poon et al., 1996; Ye et al., 1996). After some pioneering studies (Mahadevan and Hall, 1990), the effect of PEG in solutions of biological macromolecules has now been thoroughly investigated (Budayova et al., 1999; Kulkarni et al., 2000; Bonneté et al., 2001; Finet and Tardieu, 2001; Tardieu et al., 2002; Vivarès et al., 2002; Finet et al., 2003; Vivarès and Bonneté, 2004). As the distance between two macromolecules becomes smaller than the polymer diameter, the PEG molecules get excluded from this region. The resulting unbalanced osmotic pressure is equivalent to a macromolecular attraction, which drives the macromolecules toward each other. Thereby, the addition of PEG may modify the phase diagram boundaries, induce either liquid-liquid or liquid-solid phase separations and act on the kinetics of the process, e.g., on the precipitation/nucleation rate (Galkin and Vekilov, 2000), as observed with Brome Mosaïc virus (BMV) in previous studies. Indeed, the phase diagrams determined with microbatch experiments with either PEG 8000 or PEG 20,000 (Casselyn et al., 2001) showed essentially three phases. The solubility curve delineates, as usual, the region where the solution is undersaturated and the virus soluble, and the region of supersaturation where the growth of large crystals may

Submitted March 2, 2004, and accepted for publication July 19, 2004.

Address reprint requests to Dr. Stéphanie Finet, ESRF, BP 220, 38043 Grenoble Cedex, France. Tel.: 33-476-88-2682; Fax: 33-476-88-2325; E-mail: finet@esrf.fr.

0006-3495/04/10/2737/12 $2.00

doi: 10.1529/biophysj.104.042036

occur. When the PEG concentration increases, the depletion attraction becomes stronger and leads to a phase separation, which in our case results in the precipitation of microcrystals. At a given pH, the phase transition boundaries have been observed to shift as a function of the PEG molecular weight. Finally, the making of a stable crystal requires in addition the formation of specific contacts, which generally imply some dehydration. So far, the building of crystallographic symmetry has remained largely unknown (Wukovitz, 1996). The massive formation of microcrystals at high PEG concentration was an opportunity to understand more about the early steps of crystal nucleation and growth.

On the experimental side, despite the number of attempts, only in a few cases have putative nuclei been observed (Yau and Vekilov, 2000, 2001; Petsev et al., 2003). On the theoretical and computational sides, however, many studies have been performed that yielded hypotheses on the nucleation pathway.

Classical nucleation theory assumes that the critical nuclei should have a spherical shape, due to the surface tension, with the same crystalline organization as in the stable bulk crystal (Boistelle and Astier, 1988; ten Wolde and Frenkel, 1997). The critical nucleus is characterized by its radius, R_c, the value of which depends upon the solution supersaturation $\sigma = \ln(c/c_s)$ (where c is the concentration and c_s the solubility of the protein), and on the physicochemical conditions. The nucleus will tend to redissolve if it loses a molecule, whereas the binding of a molecule will trigger the nucleus growth. Computer simulations for globular proteins (ten Wolde and Frenkel, 1997; Oxtoby, 1998; Talanquer and Oxtoby, 1998) introduced the notion of a metastable critical point that depends on a critical crystallization temperature T_c, where the free-energy barrier is the lowest for nucleation and leads to optimal crystal growth. Close to this point, an amorphous critical nucleus would consist in the disordered aggregation of a few molecules, and the crystallinity would appear later during the growth process. By varying the temperature and thus moving away from T_c, the free-energy barrier increases, still allowing nucleation, yet with nuclei having the same organization as in the crystal.

Experimentally, critical nuclei are not easily accessible. Light scattering has been used to investigate the early steps of nucleation of some globular or spherical macromolecules, yet far from phase separation, i.e., in solution conditions where only a small number of nuclei can grow into observable crystals. The idea was to look for the formation of aggregates that could be the desired critical nuclei (Malkin and McPherson, 1994). Among them, Satellite Tobacco Mosaïc virus (STMV), a spherical plant virus of 160 Å in diameter, and apoferritin, a quasispherical protein of 130 Å in diameter, were studied. Aggregates were indeed observed, and their evolution was followed as a function of the supersaturation σ. The critical radius was assumed to be the radius of the aggregates measured when crystals started to be visible in the solution. In the case of STMV, for $\sigma = 1$–1.4, R_c was in the range of 30–50 nm corresponding to 7–30 STMV particles. For apoferritin, R_c was in the range of 40–50 nm, and the nuclei were thus thought to be composed of 30–70 apoferritin monomers. However, one difficulty is that there is no proof that the aggregates studied with light scattering are the nuclei that yield crystals. Moreover, light scattering cannot tell us whether the aggregates are amorphous or crystal-like. AFM now allows us to visualize biological macromolecules at the nanometer scale. It has already been used to visualize the crystal growth process of different macromolecular crystals (Malkin et al., 1995, 1999; Li et al., 1999; Kuznetsov et al., 2000; McPherson et al., 2000; Yau et al., 2000; McPherson et al., 2001; Yau and Vekilov, 2001). In the case of apoferritin, it has also been used to observe the formation in solution of the clusters at the origin of crystals (Yau and Vekilov, 2000). In this particular case, the nuclei have a size close to that predicted by Malkin and McPherson (1994). They appear planar rather than spherical, and made of several rods of molecules with the same molecular arrangement as in the crystals.

In the present study, we performed time-resolved small-angle x-ray scattering (SAXS) experiments on the ID2 beamline of the European Synchrotron Radiation Facility (ESRF) to follow the formation of BMV microcrystals. Preliminary results of these experiments were presented elsewhere (Casselyn et al., 2002). The beamline is equipped with a fast two-dimensional detector and a stopped-flow device (Narayanan et al., 2001) that permitted the rapid mixing of three components (virus, PEG, and solvent) and injection under the x-ray beam. The precipitation of the viral solutions at various concentrations was induced by the use of three PEGs of different molecular weight, 3350 Da, 8000 Da, or 20,000 Da, at pH 5.9 and room temperature. The 50-ms-long measurements were carried out with exponentially spaced intervals from 180 ms after the mixing up to 10 or 25 min, according to the sample composition. These experiments allowed us to follow the kinetics of early growth of BMV microcrystals as a function of the PEG size and concentration.

MATERIAL AND METHODS

Sample preparation

BMV was purified from infected barley leaves as previously described (Casselyn et al., 2001), and concentrated at 40 mg/ml. The virions were maintained in their storage 20 mM Na acetate (Calbiochem, EMD Biosciences, San Diego, CA) buffer, at pH 5.9. All the experiments were undertaken at constant pH, and at 15°C. Three PEGs of molecular weights 3350 Da, 8000 Da, and 20,000 Da from Hampton Research (Riverside, CA) were used, called in the following PEG 3 K, 8 K, and 20 K. The solutions at concentrations 5%, 10%, and 20% (w/v) were also maintained in 20 mM Na acetate, pH 5.9.

Stopped-flow device

The stopped-flow device (Bio-Logic Science Instruments, Grenoble, France) available on ID2 is composed of three tanks, permitting the rapid mixing, between 3 and 10 ms, of the different components and the pushing of the sample toward a 1.5-mm internal diameter quartz capillary. Two tanks were filled respectively with the diluting 20 mM Na Acetate buffer at pH 5.9, and with the PEG solutions. The third tank contained the BMV solution at a concentration of 40 mg/ml. A software (Bio-Logic Science Instruments) permitted the definition and the mixing of the desired volumes. The final concentrations obtained were 20, 10, 5, or 2.5 mg/ml virus, in presence of 10, 5, or 2.5% (w/v) PEG. The experiments were found reproducible provided that the volumes injected were large enough. The total injected volume of the samples was 80 μl, except for the samples at 2.5 mg/ml BMV, where the volumes were doubled. Because of the PEG viscosity, the capillary was cleaned several times by flushing with buffer before each series.

SAXS experiments

Beamline

SAXS experiments were performed on the ID2 beamline at ESRF (Grenoble, France). The operating energy was of 12.5 KeV, i.e., a wavelength of ≈ 1 Å, for a photon flux of 10^{13} photons/s and a beam size of 0.3 mm per 0.8 mm. The scattering data were recorded for scattering vector seconds ($s = 2\sin\theta/\lambda$) ranging from 1.17 10^{-3} to 3.50 10^{-2} Å^{-1}. The increment in seconds per channel was of 0.0865 $\times$ 10^{-3} Å^{-1}. The acquisition sequence followed the formula

$$t_i = t_{i-1} + t_{meas} + c^{i-2}\,\Delta t_{int},\ \text{for } i > 1 \text{ and } t_1 = 10\,\text{ms}, \quad (1)$$

where t_i is the time after the mixing, t_{meas} the duration of each measurement (50 ms) chosen to ensure a sufficient signal, c^{i-2}, and Δt_{int} is the time interval between two exposures calculated to cover the whole process with ~20 exposures, thus avoiding radiation damage; this time lapse is equal to 120 ms (Δt_{int}) between the two first measurements and is then increased by a coefficient c (equal to 1.57 or 1.6 according to the experiments). The first frame was recorded 10 ms after mixing. The second, constituting the first reliable frame, was measured 180 ms after mixing. A fast two-dimensional detector, i.e., x-ray image intensifier coupled to a charge-coupled device camera developed at the ESRF (the fast read-out and low-noise camera or FReLoN; see Narayanan et al., 2001), synchronized to the fast -beam shutter, permitted us to record two-dimensional scattering frames. All the calculations were done with the assumption that the contribution of the geometry of the x-ray camera to the peak width can be neglected.

SAXS data reduction

The raw two-dimensional data reduction, necessary to obtain the normalized intensity values (one-dimensional data) as a function of the scattering vector seconds, consist of

1. Subtraction of the CCD dark current.
2. Correction of the spatial distortion and the spatial inhomogeneities.
3. Calibration to the absolute intensity.
4. Normalization to the incident intensity, the transmission, and the sample thickness.
5. Azimuthal integration (Narayanan et al., 2001).

The one-dimensional scattered intensity data were subtracted for corresponding buffer signal. Note that all the scattering curves are on the same scale.

THEORETICAL BASIS

Nucleation

The driving force for nucleation and growth is the difference between the chemical potential of a macromolecule in the crystalline state and in solution. It is usually written as

$$\Delta\mu = k_B T \ln(c/c_s), \quad (2)$$

where c is the macromolecular concentration before nucleation, c_s is the solubility (i.e., the concentration at saturation), k_B is the Boltzmann's constant, T is the temperature, and $\sigma = \ln(c/c_s)$ is the supersaturation. By definition, a nucleus is a thermodynamically unstable assembly that can either decay back into monomers or continue to grow into a crystal. The energy required to form a nucleus of volume V and area S is given by

$$\Delta G = -(V/\Omega)k_B T\,\sigma + S\gamma, \quad (3)$$

where Ω is the volume of the macromolecule inside the crystal, and γ is the interfacial free energy per unit area between nucleus and solution. The first term in Eq. 3 is a volume term, where V/Ω is the number of macromolecules inside the nucleus. The second term is the energy required to create the nucleus surface. Because of the opposite effect between volume and surface term ΔG passes through a maximum for a ''critical'' size of the nucleus, at a given temperature and supersaturation ratio. If we consider a spherical nucleus, the critical radius is equal to

$$r^* = 2\Omega\gamma/k_B T\,\sigma. \quad (4)$$

When the nucleus reaches this critical radius, the corresponding free energy for nucleation is

$$\Delta G^* = 16\pi\Omega^2\gamma^3/3(k_B T\,\sigma)^2, \quad (5a)$$

or

$$\Delta G^* = (1/3)(4\pi r^{*2}\,\gamma). \quad (5b)$$

X-ray scattering analysis

With monodisperse solutions of globular macromolecules in aqueous buffer, the x-ray scattering curves (subtracted for background), $I(c,s)$, may be written as the product of the particle concentration by a form factor, $I(0,s)$ (scattered intensity of one particle), and by a structure factor, $S(c,s)$, which takes into account departures from ideality, owing to particle-particle interactions (Tardieu, 1994),

$$I(c,s) = c\,I(0,s)\,S(c,s). \quad (6)$$

$I(0,s)$ and $S(c,s)$ are the Fourier transforms of the spherically averaged autocorrelation functions, respectively, of the electron density contrast associated with the particle, and of the particle distribution function, which is the probability to find two particles at a distance r. The form factor gives information on the particle shape, including its oligomeric state. Then, the variation of the SAXS scattering curves as a function of particle concentration readily indicates the type of interactions, repulsive and attractive, present in solution. With repulsive interactions, the particles are evenly distributed and the structure factor at the origin, $S(c,0)$, is <1. With attractive interactions, fluctuations in the particle distribution are observed and $S(c,0)$ is >1. In a typical experiment, the form factor is measured at low protein concentration and the structure factor is then obtained by dividing the intensity curve recorded at high concentration by the form factor.

In a multicomponent system (Guinier and Fournet, 1955), the total scattered intensity becomes

$$I(c,s) = \sum_i \sum_j \sqrt{c_i c_j}\sqrt{I_i(0,s) I_j(0,s)} S_{ij}(c,s), \qquad (7)$$

where the $S_{ij}(s)$ are the partial structure factors, which take into account spatial correlations and thus interactions between particles. Therefore, in the binary mixture obtained after addition of PEG to the virus solution, the intensity becomes

$$\begin{aligned} I(c,s) = {} & c_v I_v(0,s) S_v(c,s) \\ & + 2\sqrt{c_v c_{PEG}}\sqrt{I_v(0,s) I_{PEG}(0,s)} S_{vPEG}(s) \\ & + c_{PEG} I_{PEG}(0,s) S_{PEG}(c,s), \end{aligned} \qquad (8)$$

where v stands for virus. Yet, the PEG scattering (third term) can be ignored since, when the background is recorded with the proper amount of PEG, the third term is part of the background and is subtracted with it. The cross term, although non-zero, is at most 1% of the first one since the intensity at the origin is proportional to the molecular weight and to the square of the electron density contrast. As the molecular weight of BMV is between 230 and 1500 times larger than the PEGs used, the cross term can be neglected. The scattered intensity (Eq. 8) therefore simplifies to the first term, i.e., the virus scattering.

After addition of increasing amounts of PEG to the system of volume V_S, phase separation into one liquid phase of volume V_1 depleted in virus and enriched in PEG, and one solid phase of volume V_2 enriched in virus and depleted in PEG, then occurs. The sample scattering then becomes the sum of the scattering of the individual phases. For the reasons given above, the PEG scattering can still be neglected and the scattering may be simply written as

$$I(c,s) = \left(c_1 \frac{V_1}{V_S}\right) I(0,s) S_1(c_1,s) + \left(c_2 \frac{V_2}{V_S}\right) I(0,s) S_2(c_2,s), \qquad (9)$$

where the subscripts *1* and *2* stand for each of the two phases and c_1 and c_2 for the virus concentrations in phases *1* and *2*, respectively, with $cV_S = c_1V_1 + c_2V_2$. Note, however, that c_1V_1, c_2V_2, $S_1(c_1,s)$, and $S_2(c_2,s)$ vary as a function of time after mixing. In the liquid phase, since the initial virus concentration is small and then decreases as a function of time, $S_1(c_1,s)$ remains close to 1—except perhaps at very small angles. In the solid phase, amorphous nuclei, if any, should scatter as a concentrated liquid phase and $S_2(c_2,s)$ should present an interference ring at a value of s close to the inverse of the virus diameter.

As soon as the nuclei become periodically ordered, $S_2(c_2,s)$ is no longer a continuous function. The reciprocal space is made of the (hkl) nodes of the reciprocal space of the crystal lattice. Yet, because of the finite size of the crystals, each node can be described as a delta function convoluted by the Fourier transform of the crystal shape, FT_{SHAPE}. The corresponding intensity is $(\delta_{hkl} * FT_{SHAPE}(t))^2$. It is convenient in such calculations to assume a Gaussian shape, since the Fourier transform of a Gaussian function is also a Gaussian function and where the width of the Bragg peaks decreases with crystal growth, i.e., with increasing crystal size. The intensity at the nodes is proportional to the crystallographic structure factors $|F|^2(hkl)$. Whenever one of the microcrystals is correctly oriented, a Bragg peak is observed on the detector. As soon as enough microcrystals have been formed, the x-ray diagram becomes equivalent to a powder diagram. The spherically averaged intensity may then be written as

$$\begin{aligned} I(c,s) = {} & \left(\frac{c_1V_1(t)}{V}\right) I(0,s) + \alpha(t)(\delta_{hkl} \\ & * FT_{SHAPE}(t))^2 |F(hkl)|^2 \left(c - \frac{c_1V_1(t)}{V}\right) I(0,s), \end{aligned} \qquad (10)$$

where the proportionality constant, α, accounts for the scattering efficiency of the crystals, given the geometry of the camera and the crystal shapes.

The analysis of the scattering curves should therefore help us to analyze the first steps of crystal nucleation and growth. Eq. 10, however, shows that nucleation and growth may be difficult to disentangle, since they both lead to a decrease of the virus concentration in the liquid phase. Note that the peak shape only depends upon crystal growth and that, at the end of the process when the system is in equilibrium, the virus concentration in the liquid phase, c_1, is equal to the virus solubility, c_s.

RESULTS

X-ray scattering experiments

The experiment is illustrated in Fig. 1, where the top of the figure represents the characteristic two-dimensional patterns of viruses in solution as observed on the screen during the

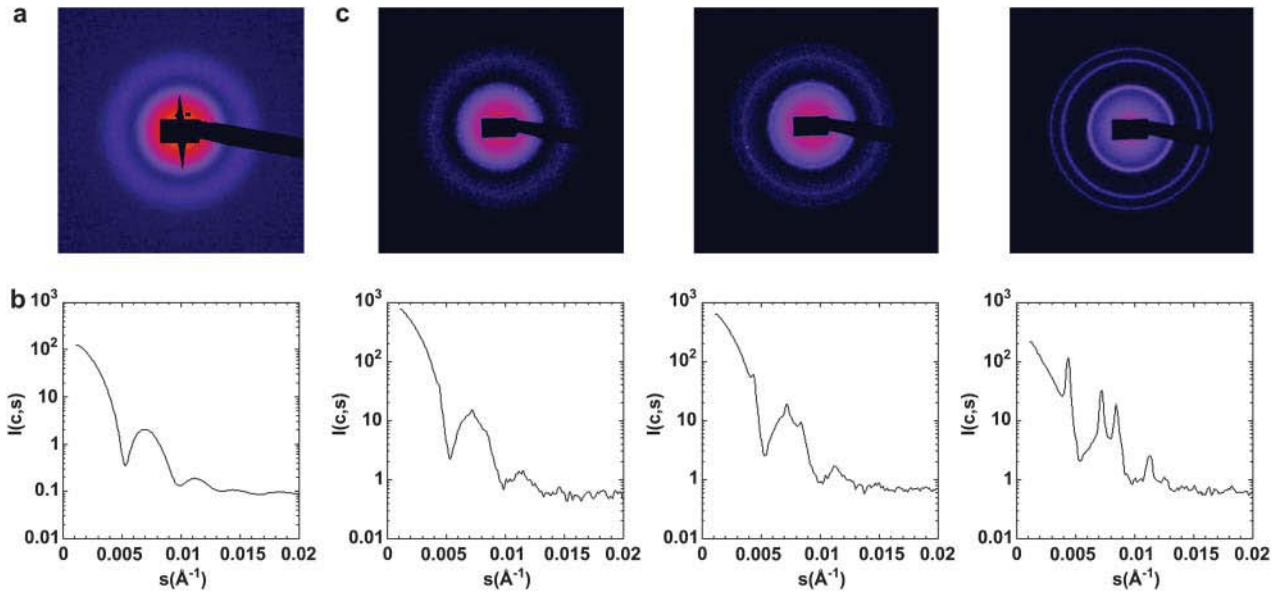

FIGURE 1 (*Top*) Characteristic two-dimensional patterns. (*Bottom*) Corresponding normalized intensity scattering curves. (*a*) Static x-ray experiment: average of 20 two-dimensional scattering patterns (each 50 ms) of a 2.5 mg/ml BMV sample. (*b*) Experimental form factor $I(0,s)$ of the BMV obtained from the less concentrated sample (2.5 mg/ml) for $1.17\ 10^{-3} < s < 4.62\ 10^{-3}$ Å^{-1}, and from the 10 and the 20 mg/ml for the $s > 4.62\ 10^{-3}$ Å^{-1} (average of 20 frames of 50 ms). (*c*) Example of a kinetic experiment with a sample containing 10 mg/ml BMV and 5% PEG 20 K (w/v). The three frames, chosen from a series of 20 frames (50 ms of acquisition time), were recorded respectively as 180 ms, 5 s, and 1511 s (~25 min) after the mixing. (*Top*) Progressive formation of diffraction rings. (*Bottom*) The corresponding normalized intensity scattering curves show the appearance of Bragg peaks.

experiment, and the bottom of the figure is the corresponding scattering spectrum after data reduction and background subtraction. As a first step, the virus scattering was measured as a function of the virus concentration without PEG (Fig. 1 *a*) to determine the form factor (Fig. 1 *b*). At the pH used for the experiments, 5.9, the interactions are only slightly repulsive and the structure factor departs from 1 only at low angles. Therefore, at low angles ($1.17\ 10^{-3} < s < 4.62\ 10^{-3}$ Å^{-1}), the signal of the less-concentrated sample (2.5 mg/ml) was taken as the form factor of the virus. At larger angles, the signal scattered by the 10 and 20 mg/ml BMV solutions was used to complete the form factor, to improve the signal/noise ratio in this region. It has been shown previously (Casselyn et al., 2001) that the form factor could be accounted for by a hollow sphere of external and internal radius of 132 and 40.5 Å, respectively.

Yet the purpose of this study was to couple time-resolved x-ray scattering and stopped-flow experiments to follow the first steps of the PEG-induced BMV nucleation and growth. The PEGs 3 K, 8 K, and 20 K were used at three different concentrations 2.5, 5, and 10% w/v, in samples containing 2.5, 5, 10, and 20 mg/ml BMV. All these concentrations were controlled through the stopped-flow device. For each condition, 20 frames were successively recorded, exponentially spaced in time (see Eq. 1). The conditions were repeated at least twice to verify the reproducibility.

Fig. 1 *c* illustrates a typical time evolution of the two-dimensional scattering patterns (*top*) and the corresponding scattering intensities (*bottom*). The top of the figure shows 50-ms spectra recorded at respectively 180 ms, 5 s, and 25 min after the mixing of BMV with PEG. The first spectrum is hardly distinguishable from that in Fig. 1 *b*. The only difference is the presence of a few diffraction spots owing to a few microcrystals remaining from the previous shot and that can never be totally eliminated despite extensive rinsing. After ~1 s, individual spots, i.e., Bragg peaks that testify to the crystal nucleation, start to appear as can be seen on the second spectrum of Fig. 1 *c*. After 20–60 s, the diffraction spots corresponding to an increasing number of randomly oriented microcrystals have merged to build the diffraction rings of a crystal powder diagram as seen on the third spectrum of Fig. 1 *c*. This simple visual report of the experiments tends to indicate that only two phases are observed, the solution or the crystal. Indeed, in no case could the presence of an interference ring, that would be the signature of an amorphous intermediary state, be detected.

As shown in Table 1, which summarizes the mixtures tested, nucleation readily occurs with BMV concentrations of 5 mg/ml with 10% PEG 20 K but requires higher BMV concentrations at 10% PEG 3 K. As expected, the solubility curves are displaced toward lower virus concentrations when the PEG size increases. Three sets of representative data were selected, one for each PEG, that are represented in Fig. 2, *a–c*, where the evolution of the scattered intensity as a function of time is readily visible. Each diffusion/diffraction dataset was then divided by the form factor of the virus, to obtain the structure factor of the sample that corresponds to the distribution of the BMV particles (see

TABLE 1 Conditions of PEG and BMV mixtures

BMV concentration	PEG 20 K 2.5%	PEG 20 K 5%	PEG 20 K 10%	PEG 8 K 2.5%	PEG 8 K 5%	PEG 8 K 10%	PEG 3 K 2.5%	PEG 3 K 5%	PEG 3 K 10%
20 mg/ml	L	yes	yes	no	yes	yes	no	L	yes
10 mg/ml	no	yes	yes	no	yes	yes	no	no	yes
5 mg/ml	no	L	yes	no	L	yes	no	no	L
2.5 mg/ml	no	no	L	no	no	L	no	no	no

PEG and BMV mixtures tested. The terms *yes* and *no* indicate the samples where diffraction peaks are or are not observed after mixing; *L* stands for limit.

Eqs. 9 and 10). In this way, the contribution of the virus shape to the signal was removed and the other signals were emphasized. The resulting curves are represented on Fig. 2, *d–f*. As can be seen on the figures, the division by the form factor made clearer the diffraction peaks, without revealing any other signal, and provided at small angles, up to $s = 0.004$ Å^{-1}, plateau-like curves. The lessening of these plateaus is directly correlated to the decrease of the concentration of soluble BMV in solution. Note, however, that the peak heights sometimes decrease at the end of the experiment, as some microcrystals sediment at the bottom of the capillary, outside of the x-ray beam. Indeed, this decrease of the peak height is not due to a partial remixing of the microcrystals, as no increase of the plateau signal due to soluble viruses can be seen.

Four series of experiments were selected for more quantitative analysis, as shown on Fig. 3, *top left*, 10% PEG 3 K, 20 mg/ml BMV; Fig. 3, *top right*, 10% PEG 8 K, 10 mg/ml BMV; Fig. 3, *bottom left*, 5% PEG 20 K, 10 mg/ml BMV; and Fig. 3, *bottom right*, 5% PEG 20 K, 20 mg/ml BMV. The diffraction peaks emerged at nearly the same positions, whatever the PEG size and BMV concentration and were numbered as indicated in Fig, 3, bottom left. The next step was therefore to check that only one crystal phase was present and to determine the crystal lattice. As can be seen on Figs. 2 and 3, the peaks were found to be better defined with PEG 20 K than with PEG 3 K or 8 K (Fig. 2 *f* and Fig. 3, *bottom left* and *bottom right*).

Seven peaks can be easily identified. Four main maxima are visible in all conditions. They are localized respectively at $s = 0.00445$ Å^{-1}, 0.00722 Å^{-1}, 0.00852 Å^{-1}, and 0.0113 Å^{-1}. With BMV concentrations ≥5 mg/ml, it is readily visible that the first and third maxima have a shoulder at $s = 0.00506$ Å^{-1} and 0.00887 Å^{-1}, respectively, and that the fourth maximum is a double peak. An eighth peak sometimes emerges from the noise at $s = 0.0125$ Å^{-1}. The intensity, width, and center of the diffraction peaks were obtained from a fit with a Gaussian bell curve. The similar growth with time of these peaks confirms that they all belong to the same phase. The spacing of the clearly defined diffraction peaks enabled us to determine the crystalline lattice of the microcrystals. A linear regression showed that the spacing follows the ratios $\sqrt{3}$, $\sqrt{4}$, $\sqrt{8}$, $\sqrt{11}$, $\sqrt{12}$, $\sqrt{19}$, $\sqrt{20}$, and $\sqrt{24}$ (see Table 2) which is consistent with a face-centered cubic lattice. One peak is missing (the peak corresponding to the $\sqrt{16}$ reflection), yet its position corresponds to the second zero of the virus form factor. The unit cell size would then be 391 Å, and considering that in the face-centered cubic system molecules are in contact with each other, the calculation of the diagonal of the faces reveals a diameter of 276 Å for the BMV particles in the cell. This value is slightly higher than the mean diameter of 264 Å obtained previously by fitting with a hollow-sphere model the experimental form factor of the virus at pH 5.9 (Casselyn et al., 2001), and probably reflects the presence of capsomers at the virus surface.

As a conclusion of this part, all the features of the scattering curves when divided by the form factor, i.e., the plateau at low angles and the series of growing peaks, consistent with Eq. 10, definitively confirm that nothing but soluble viruses and microcrystals can be detected by x rays in the samples during the time-resolved experiments. The next step was to analyze the critical nucleus, and then the evolution with time of each of the two phases.

The critical nucleus

For crystals large enough to be considered as infinite, the diffracted intensity is a set of δ-functions at the nodes of the reciprocal space. When the crystal shape is of finite size, the crystal can be described in real space by the product of the infinite crystal by a shape function, which is equal to 1 inside the crystal and 0 outside. The scattered amplitude at each node, s_{hkl}, of the reciprocal space is therefore the convolution product of a δ-function by the Fourier transform of the crystal shape. The intensity around the node may therefore be written as

$$I(s) = I_{hkl} \exp(-(4/3)\pi^2 R_g^2 (s - s_{hkl})^2), \qquad (11)$$

where R_g is the radius of gyration of the volume occupied by the crystal.

A Gaussian shape was indeed found adequate to account for the scattered intensity around each node. The parameters of the Gaussian peak were determined using the program PeakFit (SYSTAT Software, Erkrath, Germany), according to

$$I(s) = I_{hkl} \exp(-(1/2)((s - s_{hkl})/\sigma_1)^2), \qquad (12)$$

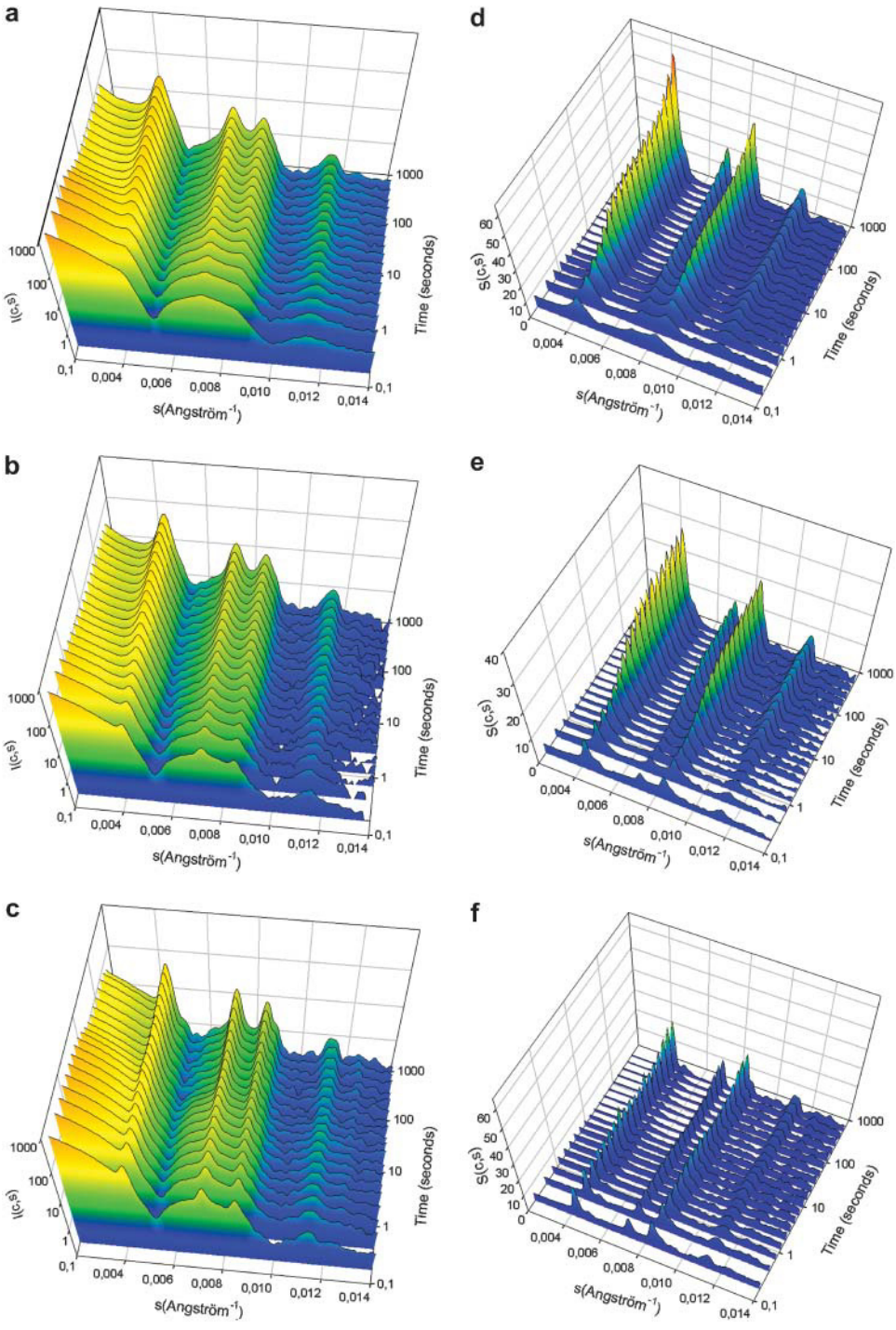

FIGURE 2 Diffraction peaks formation as a function of time (indicated in seconds) and of PEG molecular weight at concentration 10% (w/v). The labels (*a*), (*b*), and (*c*) represent, respectively, the diffracting data of samples containing PEG 3 K in the presence of 20 mg/ml BMV, PEG 8 K in presence of 10 mg/ml BMV, and PEG 20 K in presence of 10 mg/ml BMV. Note that for PEG 20 K and to a lesser extent for PEG 8 K a few peaks are already present at the beginning of the kinetic experiment, because of microcrystals stuck to the capillary from the previous run. The characteristic lobes of the scattering of soluble viruses are still visible. The labels (*d*), (*e*), and (*f*) are the corresponding structure factors (the scattered intensity divided by the form factor, to remove the scattering signal of the virus shape and improve the visibility of the peaks). Noteworthy is the fact that the width of the diffraction peaks decreases with increasing the PEG molecular weight.

where s_{hkl} is the center of the Gaussian peak and σ_I its standard deviation.

Therefore one has the relationship

$$R_g = \left(\sqrt{\frac{3}{8\pi^2}}\right)\left(\frac{1}{\sigma_I}\right). \quad (13)$$

In this expression, R_g represents the radius of gyration of the average of the individual microcrystal volumes. The relationship between this radius of gyration and the average crystal size depends upon the crystal size distribution and the crystal geometry. If we assume that R_g gives an estimate of the average radius of the individual microcrystals, then the average size D of the crystals is given by the relationship

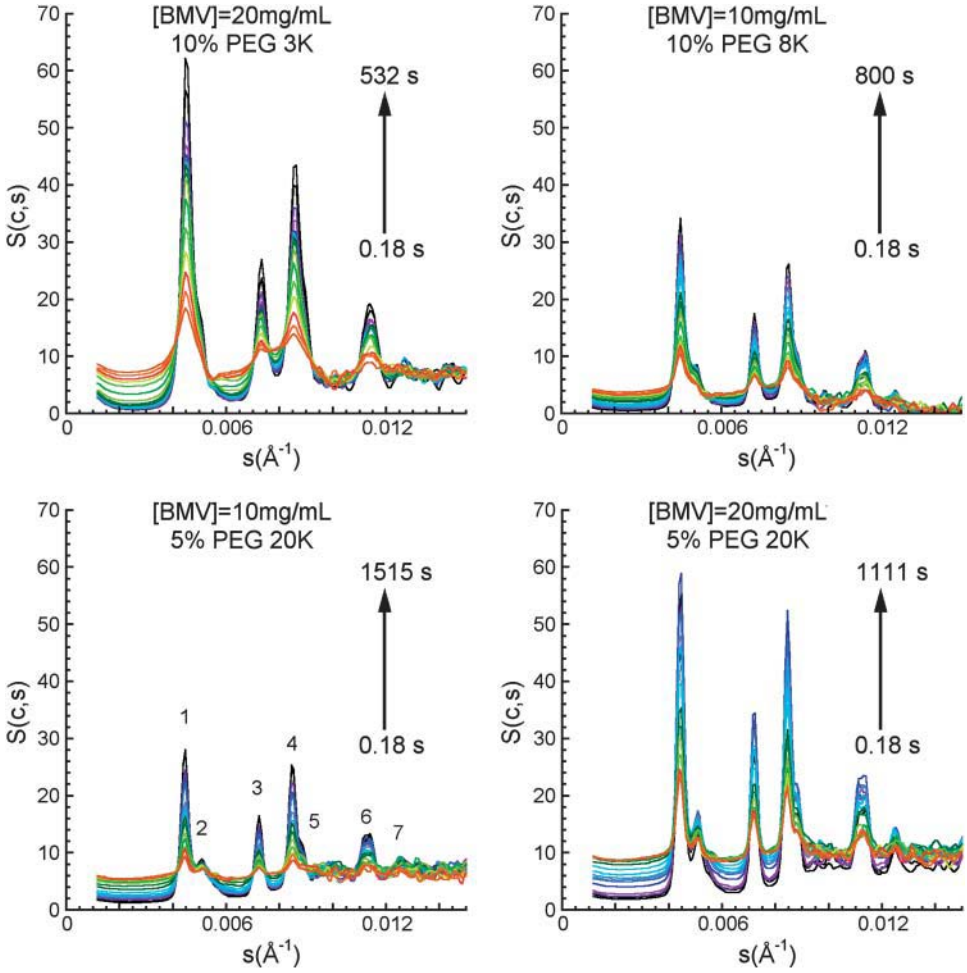

FIGURE 3 Evolution of the diffraction peaks as a function of time, for samples containing (*top left*) 10% PEG 3 K, 20 mg/ml BMV; (*top right*) 10% PEG 8 K, 10 mg/ml BMV; (*bottom left*) 5% PEG 20 K, 10 mg/ml BMV; and (*bottom right*) 5% PEG 20 K, 20 mg/ml BMV. The refinement of the peaks is visible on top-left panel. The peaks are numbered as a function of their position on bottom-left panel (see text).

$$D \approx 2R_g = \left(\sqrt{\frac{3}{2\pi^2}}\right)\left(\frac{1}{\sigma_I}\right). \quad (14)$$

The evolution of the R_g as a function of time corresponding to the four conditions shown in Fig. 3 is plotted in Fig. 4. That way, the microcrystal radius of gyration R_g was found to vary from 515 Å to 1100 Å when using PEG 3 K (Fig. 4, *top left*) and from 1000 Å to 1390 Å when using PEG 8 K (Fig. 4, *top right*). With the PEG 20 K, we observed no evolution of the radius of gyration with time, but the R_g varies from 1400 Å to 1530 Å depending upon the virus concentration (Fig. 4, *bottom left* and *bottom right*). It may seem surprising that the sizes observed are larger with increasing PEG size, where the supersaturations are larger and therefore the critical nuclei should be smaller. Yet, the growth rate of the microcrystals also increases with supersaturation so that with PEG 8 K and PEG 20 K we should observe already a mixture of nucleation and growth. Probably, the growth after nucleation is too fast to be followed and once formed, each microcrystal rapidly reaches its final size. Of course the size of the critical nuclei may be smaller than the size of the first microcrystals that are detected in the experiment, whereas the real average final size of the microcrystals may be larger (which is probably the case of Fig. 4, *bottom left* and *bottom right*, where the larger microcrystals have settled out of the x-ray beam). Therefore, the size of the critical nuclei should be equal to or

TABLE 2 Crystalline lattice of the BMV microcrystals

Reflections permitted for a face-centered cubic system	*s*-Values observed	s_R	Peak
(111) $\sqrt{3}$	0. 00445	0.00443	1
(200) $\sqrt{4}$	0.00506	0.00511	2
(220) $\sqrt{8}$	0.00722	0.00723	3
(311) $\sqrt{11}$	0.00852	0.00847	4
(222) $\sqrt{12}$	0.00887	0.00886	5
(400) $\sqrt{16}$	~0.01	0.01024	—
(331) $\sqrt{19}$	0.01120	0.01115	}6
(420) $\sqrt{20}$	0.01138	0.01147	
(422) $\sqrt{24}$	0.01250	0.01253	7

S_R are the *s*-values obtained with a linear regression $\Delta s = 0.0865\ 10^{-3}$ Å^{-1} (based on the positions of the peaks reported on Fig. 3, *bottom left*).

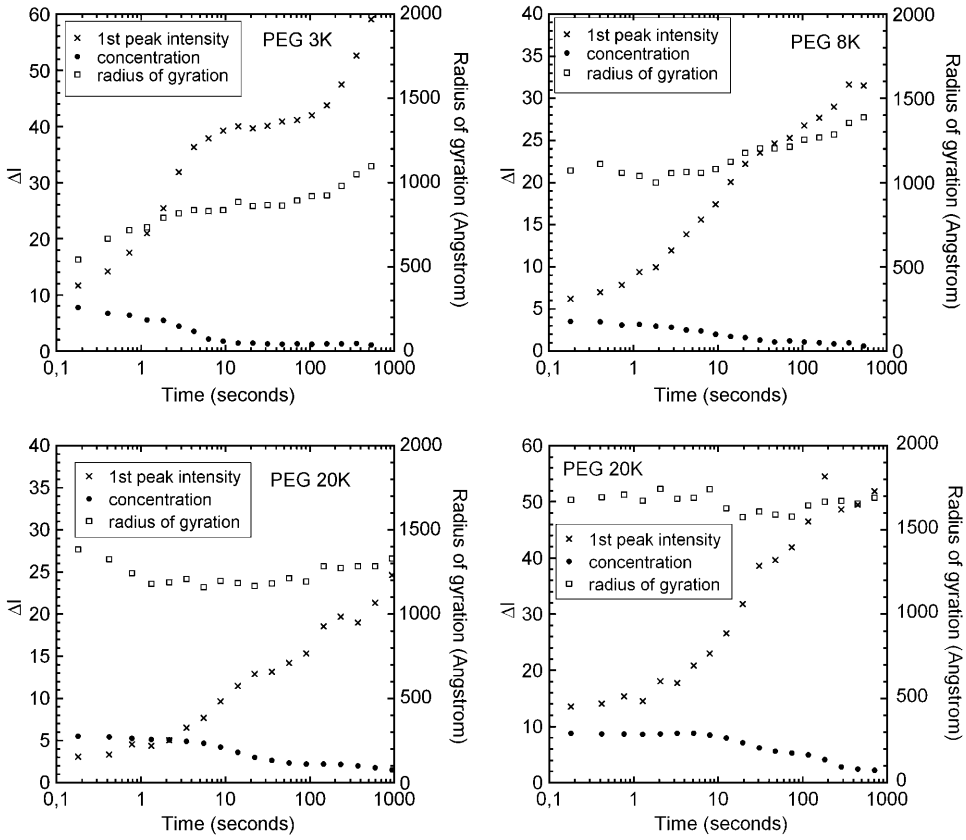

FIGURE 4 Evolution as a function of time of the intensity of peak #1, of the concentration of soluble virus (measured from the plateau level) and of the microcrystal radii of gyration (calculated from the peak width according to Eq. 13) for the spectra shown in Fig. 3. (*Top left*) 10% PEG 3 K, 20 mg/ml BMV; (*top right*) 10% PEG 8 K, 10 mg/ml BMV; (*bottom left*) 5% PEG 20 K, 10 mg/ml BMV; and (*bottom right*) 5% PEG 20 K, 20 mg/ml BMV.

smaller than the smallest size observed in our experiments, i.e., a radius of gyration of ~515 Å. Taking 276 Å as the virus diameter and assuming that 70% of the nucleus volume is occupied by the virus (in the face-centered cubic system), one therefore obtains that the smallest spherical microcrystal contributing to diffraction in Fig. 4, *top left*, is made of ~36 viruses. The number of viruses in the (possibly nonspherical) critical nucleus is ≤36. Such a size, coupled to the solubility c_s (~2.5 mg/ml for 10% PEG 3 K), allows us to estimate the interfacial free energy. One obtains $\gamma \leq 6.25\ 10^{-5}\ k_BT/Å^2$ from Eq. 4 and the critical activation free energy ΔG is found ≤65 k_BT from Eq. 5b. These low values are consistent with the rapid nucleation and growth obtained at the phase separation.

Kinetics of crystal nucleation and growth

Microcrystal nucleation and growth can be quantified by studying the evolution of the diffracting signal and the consumption of free BMV. These parameters were analyzed as a function of BMV concentration, PEG molecular weight, and concentration, and are also represented on Fig. 4.

The kinetics of formation of the microcrystals can be followed by considering the evolution as a function of time of the intensity and shape (width) of the resulting diffraction peaks. Moreover, as the intensity near the origin is representative of the concentration of soluble virus in solution, the initial plateau value corresponds to the actual BMV concentration in the mixture at the beginning of the experiment, whereas the final plateau value is close to the virus solubility c_s, i.e., from 0.1 to 1 mg/ml for 10% PEG 20 K and 2–3 mg/ml for 10% PEG 3 K. As the samples could not be recovered after the stopped-flow experiments to measure the concentrations in the two phases, a few of the conditions studied were reproduced in a separate experiment, and the two phases separated by sedimentation. In a PEG 20 K BMV 20 mg/ml experiment, the measurement of the optical density of the supernatant indicated only 0.75 ± 0.25 mg/ml of BMV left in solution. The measurement of the refractive index indicated that 92 ± 6% of the PEG was in the supernatant.

The increase of the Bragg peak intensities can be directly related to two distinct events. The first one is the formation of new nuclei; the second is the growth of existing microcrystals. Both of these events imply the decrease of the concentration of soluble virus in solution, and can be followed from the values of the plateau-like curves near the origin on Fig. 3.

Nucleation processes and crystal growth obtained are not exactly similar with the three different sizes of PEG as can be seen on Fig. 4. With PEG 3 K (Fig. 4, *top left*), the kinetics clearly show a two-step process that could indicate that the nucleation phase is distinct from the growth phase. It seems

that for this PEG size, the nucleation occurs in the 12–13 s after the beginning of the experiment, after which the increase in signal is due to the diffraction of growing microcrystals. As the concentration does not seem to vary anymore, one can suppose that the increase of the diffraction signal and of the size of the crystals is due to the fusion of microcrystals.

Fig. 3, *bottom left* and *bottom right*, show that with PEG 20 K 5%, the height of the final diffraction peaks is twice higher when using 20 mg/ml BMV than when using only 10 mg/ml. This immediately reveals that the variations of the peak intensities are due to the increase of the microcrystal number rather than to the growth of existing ones (a signal proportional to the square of the number of viruses present in the crystals would then be expected). The fact that, even if the height of the diffraction peaks increases for PEGs 8 K and 20 K, no evolution of their width is observed, confirms that for both PEGs, nucleation and growth up to a final size are simultaneous. The width of the peaks remains almost constant as a function of time, but the decrease of the soluble virus concentration confirms that soluble viruses are used to form new microcrystals.

To determine the importance of the PEG concentration and molecular weight, the different results obtained for a unique concentration of virus, in presence of PEG (8 K or 20 K) at different concentrations, were compared. Since peak #3 only corresponds to the 220 reflection, it was considered to be the most relevant for direct comparison between experimental conditions. The intensity variations of peak #3 for the samples containing 10 mg/ml BMV combined with 5 or 10% (w/v) PEG are reported on Fig. 5.

As can be seen on Fig. 5, it is possible to detect the existence of a lag time for new microcrystals to appear. For both PEGs, the lag time increases with decreasing PEG concentration, from 1 s to ~8 s for PEG 8 K and from 0.5 s to ~1 s for PEG 20 K. Moreover, as can be seen on the figure, the kinetics observed for 5% PEG 20 K and 10% PEG 8 K are quite similar, indicating that a higher PEG concentration may compensate for a lower PEG size.

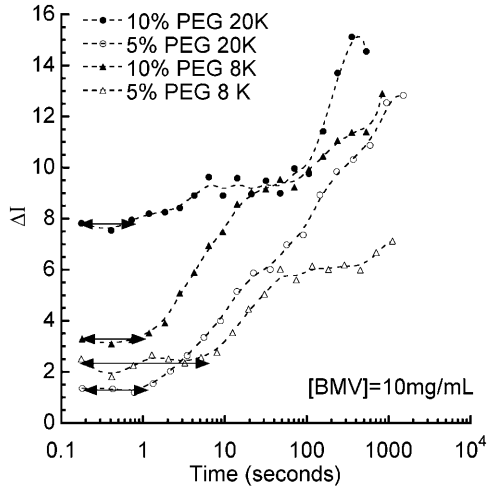

FIGURE 5 Evolution of the intensity of peaks #3 fitted by a Gaussian bell-shaped curve, for PEGs 20 K and 8 K 5% and 10% (w/v) in 10 mg/ml BMV samples. Lag times necessary for microcrystals to appear are indicated by arrows.

DISCUSSION

Time-resolved SAXS experiments allowed us to follow the formation of the microcrystalline precipitates of BMV. Owing to the stopped-flow device, the high brilliance and the CCD detector of the ID2 beamline at ESRF, the disappearance of the viruses from solution and the simultaneous growth of diffraction peaks could be observed from the beginning of crystal nucleation and growth until the end of the process when no more viruses are available for crystallization in the solution. Twenty measurements exponentially spaced in time were registered after the mixing of different volumes of BMV and PEG, from 180 ms after mixing until the end of the process, after 10–20 min.

The use of three different sizes of PEG, 3 K, 8 K, and 20 K, confirmed the efficiency of this polymer to induce phase separation and crystallization. It is better and better documented that these PEG properties directly derive from the depletion attraction induced by PEG between macromolecules. The attraction amplitude increases with the PEG concentration whereas the attraction range increases with the PEG size (Vivarès et al., 2002). In the present experiments, crystal nucleation and growth were shown to be directly driven by the strength of the attraction, e.g., at 10 mg/ml BMV concentration, experiments with 10% PEG 8 K were quite similar to those with 5% PEG 20 K (Fig. 5) confirming that a higher concentration of PEG may counterbalance a smaller size. Yet, the difference in PEG size resulted in an obvious difference in the x-ray data—the sharpness of the diffraction peaks at the onset of nucleation was observed to increase with increasing PEG size, whereas the final peak width was the same. At a given PEG concentration, the BMV concentration, which determines the supersaturation, was of course another important factor to control nucleation and growth. Finally, whatever the PEG size, at 10% PEG concentration, the BMV solubility as measured from the scattering curves at the end of the experiments was found to be quite low, varying from ~0.5 mg/ml for PEG 20 K up to 2 mg/ml for PEG 3 K.

In the best x-ray diagrams, up to eight well-differentiated diffraction peaks could be observed (Figs. 2 and 3). The positions of the four main peaks had already been determined in our previous studies at LURE (Casselyn et al., 2001), but at that time the other weaker peaks were not distinguishable, preventing an accurate determination of the crystalline lattice. The use of the ID2 beamline at ESRF with its CCD detector allowed us to obtain a higher resolution. Moreover, the division of the intensity curves by the form factor of the virus highlighted the peaks so that a face-centered cubic lattice, with a unit cell size of 391 Å (Table 2)

could be demonstrated. In fact, the value slightly varies with the PEG size, from 385 Å with PEG 3 K, to 390 Å with PEG 8 K, up to 391 Å with PEG 20 K. Since the microcrystal growth is slower with PEG 3 K than with higher sizes of PEG, the formation of better-arranged and more compact crystals might be favored. Another explanation, suggested by one of the reviewers, could be the stronger osmotic pressure applied on the crystals at constant weight fraction when decreasing PEG size. Cubic lattices are frequently observed with spherical viruses, yet the face-centered cubic lattice is particularly reminiscent of what is usually observed with colloids at the fluid-solid transition. Therefore, the BMV presents characteristics that are intermediate between proteins and colloids. The lattice observed here is, however, different from that of the crystals used for the determination of the atomic structure of BMV by McPherson's team (Lucas et al., 2001, 2002) which were obtained in different crystallization conditions and crystallized either in a rhombohedric (R3) or an orthorhombic space group ($P2_12_12_1$). None of these space groups can account for the observed data. We have reported previously (Casselyn et al., 2001, 2002) that large crystals could be reproducibly obtained in conditions just below the phase separation curve. However, high-resolution data of these crystals have not yet been obtained.

Because of the quasisynchronized formation of a large number of nuclei, the early stages of crystal nucleation and growth could be observed. The timescale of the process was easily followed, either from the decrease of the BMV concentration in solution or from the growth of the peaks, which were both representative of the early stages of crystallization. Such a timescale could not be measured in usual crystallization conditions where only a few crystals are obtained after some hours or some days. After a lag time that seemed to be a function of the supersaturation, diffraction spots became apparent on the detector and their number increased until making diffraction rings (Fig. 1, *top*). The intensity of the rings went on growing rapidly during the first minute or so and then much more slowly during ~10–20 min, until the virus left in the solution reached its solubility limit and no evolution of the intensity was further observed, except sometimes for a decrease of the diffraction signal due to the sedimentation out of the x-ray beam of the largest microcrystals. The lag time necessary for the nuclei to become visible varies from approximately half a second up to several seconds, according to the concentration of both PEG and BMV (Figs. 4 and 5). The radius of gyration of the critical nuclei was shown to be small, $\leq$500 Å. From the variation of the intensities of the diffraction peaks as a function of time, two processes were clearly visible that partially overlap—an extensive nucleation of microcrystals followed by their subsequent growth (Figs. 4 and 5). With PEG 20 K 5% the diffraction peaks evolved continuously during the experiment, to reach a final height proportional to the initial virus concentration, which indicates that the microcrystals go on forming and that the growth is limited because of the large number of nuclei. In such a case, the PEG-induced attraction, rather than the BMV concentration, appears to be the driving force for crystallization. At the end of the experiments, the limiting radius of gyration of the microcrystals was shown to vary from ~1100 to 1700 Å, according to the PEG size. We still do not know the shape of the microcrystals, but if they were spherical, they would be composed of ~350 up to 1300 BMV particles.

Finally, no intermediary state could be detected between solution and crystal, indicating structured nucleation from the very beginning. The division of the scattered intensity curves by the form factor of BMV clearly shows that only two species are present in solution, soluble BMV and microcrystals. Since the number of nuclei is so large and the nucleation process is lasting for at least 1 min, the lack of any other signal is in agreement with a nucleation pathway of BMV crystalline samples involving only periodic structures. The experiments also demonstrate that at high supersaturation nucleation can be rather fast, and does not require the preliminary formation of liquid-like droplets as proposed by ten Wolde and Frenkel (1997) near a fluid-fluid critical point.

In the colloid field, it has been shown that in mixtures of hard spheres and neutral polymers the type of phase diagram depends essentially on the ratio, ξ, of the radius of gyration of the polymer molecules to the radius of gyration of the colloidal particles. For $\xi \leq 0.25$, only two phases coexist in the phase diagram (a fluid phase and a crystal phase), whereas a triple point (gas, liquid, and crystal), is present for $\xi \geq 0.25$ (Illet et al., 1995). In the present work, ξ is <0.25 for PEG 3 and 8 K but not for PEG 20 K since the radii of gyration are, respectively, 23, 40, and 70 Å (Devanand and Selser, 1991). In the present work, only two phases were observed. Moreover, the polymer concentration range where the phase separation occurs is much lower than in the theoretical predictions. Such differences with the colloid case still remain unexplained.

The authors acknowledge the memory of Dr. Jean Witz, who initiated this work. They thank T. Narayanan for helpful discussions and the reviewers for sharp suggestions.

This work was supported by a research grant of the scientific program ''ACI Matière Complexe'' of the Centre National de la Recherche Scientifique. A.T. gratefully acknowledges the financial support of the Centre National d'Etudes Spatiales.

REFERENCES

Asakura, S., and F. Oosawa. 1958. Interactions between particles suspended in solutions of macromolecules. *J. Pol. Sci.* 33:183–192.

Boistelle, R., and J. P. Astier. 1988. Crystallization mechanisms in solution. *J. Cryst. Growth.* 90:14–30.

Bonneté, F., D. Vivarès, C. Robert, and N. Colloch. 2001. Interactions in solution and crystallization of *Aspergillus flavus* urate oxidase. *J. Cryst. Growth.* 232:330–339.

Budayova, M., F. Bonneté, A. Tardieu, and P. Vachette. 1999. Interactions in solution of large oligomeric protein. *J. Cryst. Growth.* 196:210–219.

Casselyn, M., S. Finet, A. Tardieu, and H. Delacroix. 2002. Time-resolved scattering investigations of Brome mosaïc virus microcrystals appearance. *Acta Crystallogr.* D58:1568–1570.

Casselyn, M., J. Perez, A. Tardieu, P. Vachette, J. Witz, and H. Delacroix. 2001. Spherical plant viruses: interactions in solution, phase diagrams and crystallization of Brome mosaïc virus. *Acta Crystallogr.* D57:1799–1812.

Devanand, K., and J. C. Selser. 1991. Asymptotic behavior and long-range interactions in aqueous solutions of poly(ethylene oxide). *Macromolecules.* 24:5943–5947.

Finet, S., and A. Tardieu. 2001. Alpha-crystallin interaction forces studied by small-angle x-ray scattering and numerical simulations. *J. Cryst. Growth.* 232:40–49.

Finet, S., D. Vivarès, F. Bonneté, and A. Tardieu. 2003. Controlling biomolecular crystallization by understanding the distinct effects of PEGs and salt on solubility. *In* Methods in Enzymology, Macromolecular Crystallography, Part *C*. C.W. Carter and R.M. Sweet, editors. Academic Press, San Diego, CA. 105–129.

Galkin, O., and P. G. Vekilov. 2000. Control of protein crystal nucleation around the metastable liquid-liquid phase boundary. *Proc. Natl. Acad. Sci. USA.* 97:6277–6281.

George, A., and W. W. Wilson. 1994. Protein crystallization from a dilute solution property. *Acta Crystallogr.* D50:361–365.

Guinier, A., and G. Fournet. 1955. Small Angle Scattering of X-Rays. Wiley, New York.

Illet, S. M., A. Orrock, W. C. K. Poon, and P. N. Pusey. 1995. Phase behaviour of a model colloid-polymer mixture. *Phys. Rev. E.* 51:1344–1352.

Kulkarni, A. M., A. P. Chatterjee, K. S. Schweizer, and C. F. Zukoski. 2000. Effects of polyethylene glycol on protein interactions. *J. Chem. Phys.* 113:9863–9873.

Kuznetsov, Y. G., A. J. Malkin, R. W. Lucas, and A. McPherson. 2000. Atomic force microscopy studies of icosahedral virus crystal growth. *Colloids Surf. B Biointerf.* 19:333–346.

Li, H., A. Nadarajah, and M. L. Pusey. 1999. Determining the molecular-growth mechanisms of protein crystal faces by atomic force microscopy. *Acta Crystallogr.* D55:1036–1045.

Lucas, R. W., Y. G. Kuznetsov, S. B. Larson, and A. McPherson. 2001. Crystallization of Brome mosaïc virus and $T = 1$ Brome mosaïc virus particles following a structural transition. *Virology.* 286:290–303.

Lucas, R. W., S. B. Larson, and A. McPherson. 2002. The crystallographic structure of Brome mosaïc virus. *J. Mol. Biol.* 317:95–108.

Mahadevan, H., and C. K. Hall. 1990. Statistical-mechanical model of protein precipitation by non-ionic polymer. *AIChE J.* 36:1517–1528.

Malkin, A. J., Y. G. Kuznetsov, R. W. Lucas, and A. McPherson. 1999. Surface processes in the crystallization of turnip yellow mosaïc virus visualized by atomic force microscopy. *J. Struct. Biol.* 127:35–43.

Malkin, A. J., G. Kuznetsov Yu, T. A. Land, J. J. DeYoreo, and A. McPherson. 1995. Mechanisms of growth for protein and virus crystals. *Nat. Struct. Biol.* 2:956–959.

Malkin, A. J., and A. McPherson. 1994. Light-scattering investigation of nucleation processes and kinetics of crystallization in macromolecular systems. *Acta Crystallogr.* D50:385–395.

McPherson, A., A. J. Malkin, Y. G. Kuznetsov, and M. Plomp. 2001. Atomic force microscopy applications in macromolecular crystallography. *Acta Crystallogr.* D57:1053–1060.

McPherson, A., A. J. Malkin, and G. Kuznetsov Yu. 2000. Atomic force microscopy in the study of macromolecular crystal growth. *Annu. Rev. Biophys. Biomol. Struct.* 29:361–410.

Narayanan, T., O. Diat, and P. Bösecke. 2001. SAXS and USAXS on the high brilliance beamline at the ESRF. *Nucl. Instrum. Meth. Phys. Res. A.* 467–468:1005–1009.

Oxtoby, D. W. 1998. Nucleation of first-order phase transitions. *Acc. Chem. Res.* 31:91–97.

Petsev, D. N., K. Chen, O. Gliko, and P. G. Vekilov. 2003. Diffusion-limited kinetics of the solution-solid phase transition of molecular substances. *Proc. Natl. Acad. Sci. USA.* 100:792–796.

Poon, W., P. Pusey, and H. Lekkerkerker. 1996. Colloids in suspension. *Phys. World.* 9:27–32.

Talanquer, V., and D. W. Oxtoby. 1998. Crystal nucleation in the presence of metastable critical point. *J. Chem. Phys.* 109:223–227.

Tardieu, A. 1994. Thermodynamics and structure—concentrated solutions—structured disorder in vision. *In* Neutron and Synchrotron Radiation for Condensed Matter Studies. J. Baruchel, M. S. Lehman, J. R. Regnard, and C. Schlenker, editors. Les Editions de Physique: Springer-Verlag, Heidelberg, Germany. 145–160.

Tardieu, A., F. Bonneté, S. Finet, and D. Vivarès. 2002. Understanding salt- or PEG-induced attractive interactions to crystallize biological macromolecules. *Acta Crystallogr.* D58:1549–1553.

ten Wolde, P. R., and D. Frenkel. 1997. Enhancement of protein crystal nucleation by critical density fluctuations. *Science.* 277:1975–1978.

Vivarès, D., L. Belloni, A. Tardieu, and F. Bonneté. 2002. Catching the PEG-induced attractive interaction between proteins. *Eur. Phys. J. E.* 9:15–25.

Vivarès, D., and F. Bonneté. 2004. Liquid-liquid phase separations in urate oxidase/PEG mixtures: characterization and implications for protein crystallization. *J. Phys. Chem. B.* 108:6498–6507.

Wukovitz, S., and T. O. Way. 1996. Why protein crystals favor some space groups over others. *Nat. Struct. Biol.* 2:1062–1067.

Yau, S., B. R. Thomas, and P. G. Vekilov. 2000. Molecular mechanisms of crystallization and defect formation. *Phys. Rev. Lett.* 85:353–356.

Yau, S. T., and P. G. Vekilov. 2000. Quasi-planar nucleus structure in apoferritin crystallization. *Nature.* 406:494–497.

Yau, S. T., and P. G. Vekilov. 2001. Direct observation of nucleus structure and nucleation pathways in apoferritin crystallization. *J. Am. Chem. Soc.* 123:1080–1089.

Ye, X., T. Narayanan, P. Tong, J. S. Huang, M. Y. Lin, B. L. Carvalho, and L. J. Fetters. 1996. Depletion interactions in colloid-polymer mixtures. *Phys. Rev. E.* 54:6500–6510.